Accepted Manuscript

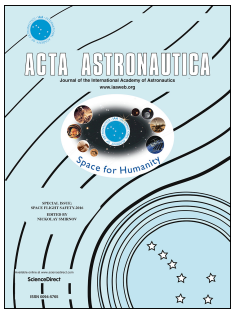

Trajectory design and guidance for landing on Phobos

Eric Joffre, Mattia Zamaro, Nuno Silva, Andrés Marcos, Pedro Simplício

PII: S0094-5765(17)30332-6

DOI: 10.1016/j.actaastro.2018.06.024

Reference: AA 6942

To appear in: *Acta Astronautica*

Received Date: 5 March 2017

Revised Date: 2 June 2018

Accepted Date: 9 June 2018

Please cite this article as: E. Joffre, M. Zamaro, N. Silva, André. Marcos, P. Simplício, Trajectory design and guidance for landing on Phobos, *Acta Astronautica* (2018), doi: 10.1016/j.actaastro.2018.06.024.

Trajectory Design and Guidance for Landing on Phobos

Eric Joffre[a,*], Mattia Zamaro[a], Nuno Silva[a], Andrés Marcos[b], Pedro Simplício[b]

[a] *Airbus Defence and Space Ltd, Gunnels Wood Road, Stevenage SG1 2AS, UK*
[b] *University of Bristol, Queen's Building, University Walk, Bristol BS8 1TR, UK*

Abstract

While common Descent and Landing strategies involve extended periods of forced motion, significant fuel savings could be achieved by exploiting the natural dynamics in the vicinity of the target. However, small bodies are characterised by perturbed and poorly known dynamics environments, calling for robust autonomous guidance, navigation and control. Airbus Defence and Space and the University of Bristol have been contracted by the UK Space Agency to investigate the optimisation of landing trajectories, including novel approaches from the dynamical systems theory, and robust nonlinear control techniques, with an application to the case of a landing on the Martian moon Phobos.

Keywords: Landing, Small Bodies, Libration Point Orbits, Invariant Manifolds, Trajectory Design, Guidance

1. Introduction

Space sample return missions have a record of revolutionising planetary science. In 2012, new chemical analyses carried out by the University of Chicago on the lunar material collected by Apollo 14 fifty years earlier brought new elements to the disputed question of the origin of the Moon, casting a new doubt on the most widely accepted *Giant Impact* theory [1]. The US manned missions to the Moon of the Apollo programme were the first missions to return extraterrestrial samples, then followed by the Soviet Luna missions, relying solely

*Corresponding author
Email address: eric.joffre@airbus.com (Eric Joffre)

on advanced robotics. Technological advances have recently enabled sample return from farther celestial bodies: NASA's Stardust mission returned cometary dust in 2006, JAXA's Hayabusa mission returned microscopic grains of asteroid material in 2010 and NASA recently launched OSIRIS-REx to collect a sample from the Bennu asteroid, with the objective to return it to Earth in 2023.

Among the future candidates for exploration missions are the low-gravity and irregularly-shaped Martian moons. In particular, Phobos is receiving significant attention from the international community both for the wide scientific interest to finally solve the unknowns surrounding the nature of its formation, and because such a precursor mission could represent the technology drive to test some key components for a future international Mars Sample Return mission. The results of the analysis on Earth of a sample from Phobos will also characterise the exploitable in-situ resources, possibly enabling to use the moon as a waypoint for the future human exploration of the Martian System.

Close proximity operations including descent and landing are critical phases for sample return missions, typically characterised by challenging propellant consumption requirements. While common descent strategies involve an extended period of forced motion, either by translating to the surface from a close hovering station-keeping point or by starting the descent from a distant orbit, significant fuel savings could be achieved by further exploiting the natural dynamics in the vicinity of the target. However, a common characteristic of the gravitational environments around asteroids and small bodies is that they are both highly perturbed and essentially poorly known, calling for the development of reliable autonomous guidance, navigation and robust control strategies.

In parallel to the European Space Agency's *Phobos Sample Return* Phase A system study, Airbus Defence and Space has been awarded a grant by the UK Space Agency to investigate innovative strategies for the optimisation and robust control of the landing trajectories, in collaboration with the University of Bristol.

2. Phobos Sample Return mission and associated constraints

2.1. Airbus Defence and Space heritage on landing and sample return missions

Landing and sample return missions to the Moon, asteroids, Mars and its moons have been studied for many years by Airbus Defence and Space. Following the successful launch of the Rosetta mission towards Comet 67P/Churyumov-Gerasimenko, some of the recent system studies conducted for the European Space Agency are illustrated on Figure 1 below ([2, 3, 4]).

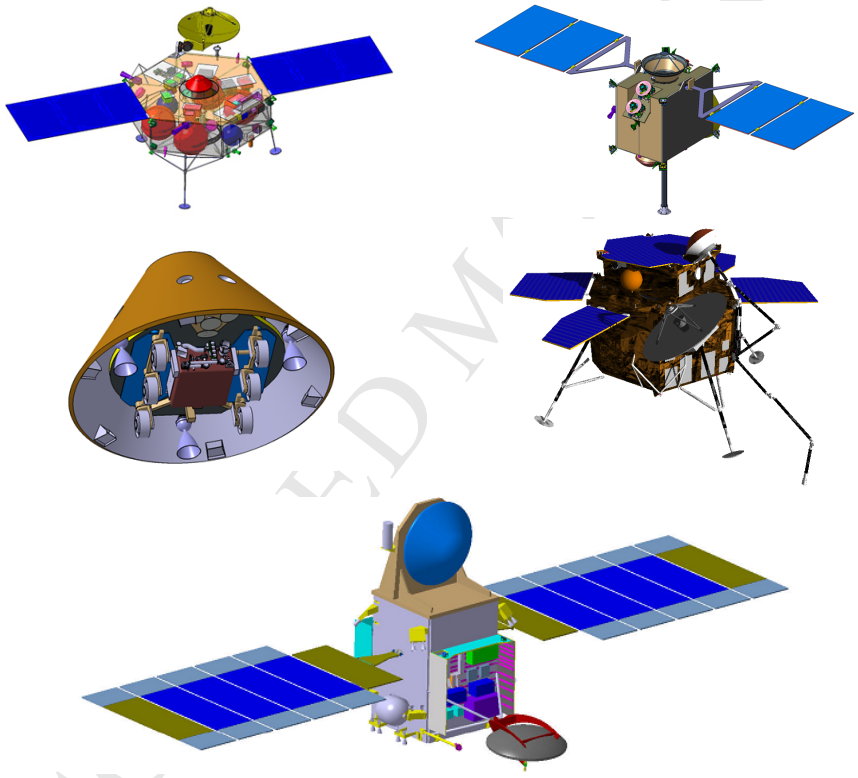

Figure 1: Airbus Defence and Space involvement in landing and sample return system studies. From left to right and top to bottom: Marco-Polo, Marco-Polo-R, Mars Precision Lander, Phootprint, Mars Sample Return Orbiter.

These projects have involved multidisciplinary teams of engineers in comprehensive system studies, thus providing a deep understanding of the constraints associated with the major subsystems for such missions, in particular:

the touch-down and landing system, the sample handling system, the Earth Re-entry Capsule (ERC), and the Guidance Navigation and Control (GNC) for proximity operations, which is the object of the study presented in this paper.

2.2. Phobos Sample Return mission overview and specific landing requirements

Phobos Sample Return is the continuation of the Phootprint pre-phase A, conducted by Airbus Defence and Space in 2014, with the renewed high-level objective to bring back 100 g of the moon surface regolith back to Earth for analysis. Reference mission scenarios and associated spacecraft designs have been baselined for the mission, including a joint ESA-Roscosmos scenario, with a Proton-M[1] launch from Baikonour in 2024 (baseline) or 2026 (backup), followed by an interplanetary transfer of about 11 months, and an ESA standalone scenario, with an Ariane 5 ECA[1] launch from Kourou in 2024/2025 (baseline) or 2026 (backup), followed by an interplanetary transfer of about 2 years. After a Mars Orbit Insertion (MOI) bringing the spacecraft into a highly elliptical orbit, a sequence of manoeuvres puts it on a Quasi-Satellite Orbit[2] (QSO) around *Deimos* for a first science phase to characterise Mars' smaller moon, orbiting the planet at about 20,000 km. Manoeuvres are then performed to reach a *Phobos* QSO, for a new characterisation phase aimed at identifying the landing sites. After a minimum of 3 fly-by trajectories for high resolution measurements of potential landing sites at low altitude (typically 5 km), the descent is initiated via a hovering point about 10 km above the surface of Phobos, for communication and navigation purposes. On Phobos' surface, images of the site are communicated to Earth for the selection of the samples, then collected by means of a robotic arm. Following ascent and return transfer, the Earth Re-entry Capsule (ERC) containing the samples is set to land in Kazakhstan or Australia.

[1] subject to launchers continued availability, as Angara-5 and Ariane 64 are planned to progressively replace Proton and Ariane 5 ECA respectively.

[2] In a three-body problem, Quasi-Satellite Orbits, also known as Distant Retrograde Orbits are 1:1 resonant orbits with the smaller primary, lying outside its Hill sphere but remaining in its vicinity following ellipse-like relative trajectories.

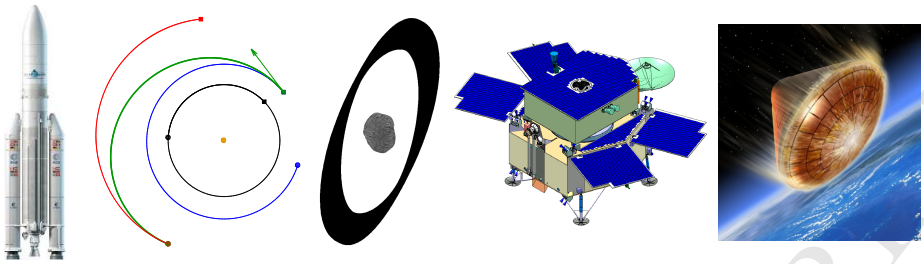

Figure 2: Phobos Sample Return main mission phases: launch and interplanetary transfer, Phobos proximity and surface operations, Earth re-entry following ascent and return transfer.

The work presented in this paper investigates alternative landing strategies that take further advantage of the natural dynamics in the vicinity of the small body. Specific requirements applicable to the landing include the following:

- 20% accessibility of Phobos surface (50% goal)
- landing accuracy on Phobos better than 50 m at a 95 % confidence level,
- landing velocities at Phobos: vertical < 1.5 m/s, horizontal < 1 m/s,
- final free-fall (no thrust) of 20 m, to avoid surface contamination.

3. Mission analysis and reference landing trajectory design

The objective of this section is to describe the dynamics environment applicable for the study, the models used for the simulations, and the derivation of reference open-loop landing trajectories.

3.1. Dynamics in the vicinity of Phobos and reference frames

Mars' largest moon Phobos is a small body with dimensions 13.1 km $\times$ 11.1 km $\times$ 9.3 km (mean ellipsoid), orbiting the Red Planet at a mean altitude of less than 6,000 km and a period of about 7 hours and 40 minutes[3]. Table 1 below

[3]shorter than the Mars rotation period: an observer on Mars would see Phobos rise in the West and set in the East.

provides some physical constants and orbital parameters[4] used in the study, both for Mars (orbit around the Sun) and Phobos [5] (orbit around Mars).

Body	Mass (kg)	sma (km)	e (-)	i (deg)
Mars	6.4185×10^{23}	227.9478×10^{6}	0.0934	0.0323
Phobos	1.0659×10^{16}	9379.2557	0.0156	0.0186

Table 1: Mars and Phobos parameters: mass, semi-major axis, eccentricity and inclination

Given the low value for Phobos' orbit eccentricity, the first level of approximation for the dynamics of a spacecraft in the Mars-Phobos system is described by the *Circular Restricted Three Body Problem* (CRTBP) [6]: even though this model is simplified, it gives some insight into the main characteristics of the dynamics. In particular, given the reduced mass ratio of $m_{\text{Phobos}}/(m_{\text{Mars}} + m_{\text{Phobos}}) = 1.65 \times 10^{-8}$, and the dimensions of Phobos, the L1 and L2 collinear Libration Points of the Mars-Phobos system lie only a few kilometers (about 3.5 km) above the surface of the moon. An important consequence of this property is that there is no possibility for a Keplerian orbit around Phobos, and the third-body perturbation of Mars gravity cannot be neglected for the design and simulation of descent and landing trajectories[5]. Figure 3 shows the location of the L1 and L2 Lagrangian points assuming a CRTBP model, together with the (in-plane) *zero-velocity curves* associated with their corresponding levels of Jacobi Integral [6].

The dominant perturbations to this model are the *ellipticity* of Phobos' orbit around Mars, and the *non-spherical gravitational field* of Phobos [7, 8]. Owing to its high inhomogeneity and very irregular shape, the gravity field of the moon cannot be described properly by a spherical (Keplerian) potential.

[4]Source: NASA JPL ephemeris at epoch 25 July 2012 00.00 UTC

[5]This property, very specific to the Mars-Phobos system, will generally not be observed in the vicinity of another small body, and in particular for an asteroid. Not only thought to be strategic for application in a future Phobos Sample Return mission, the Phobos study case has been selected as a challenging dynamical system capturing all the nonlinearity of a three body problem, to test the robustness and performance of the landing guidance and control.

Using spherical coordinates r for the radius, θ for the co-latitude, and ϕ for the longitude, and a reference radius R, the gravity potential is described by a spherical harmonics double expansion:

$$U_g(r,\theta,\phi) = \frac{\mu_{g_{\text{Phobos}}}}{R}\sum_{n=0}^{\infty}\left(\frac{R}{r}\right)^{n+1}\sum_{m=0}^{n} C_n^m(\phi)P_n^m(\cos(\theta)) \tag{1}$$

$$\text{where:} \quad \begin{cases} C_n^m(\phi) &= C_{n,m}\cos(m\phi) + S_{n,m}\sin(m\phi) \\ P_n^m(x) &= \left(1-x^2\right)^{m/2}\dfrac{d^m}{dx^m}P_n(x) \\ P_n(x) &= \dfrac{1}{2^n n!}\dfrac{d^n}{dx^n}\left(x^2-1\right)^n \end{cases} \tag{2}$$

Figure 3 below illustrates the location of the CRTBP L1 and L2 Lagrangian points, and provides the Gravity Harmonics coefficients $C_{n,m}$ and $S_{n,m}$ for a reference radius of $R = 11$ km. [9]

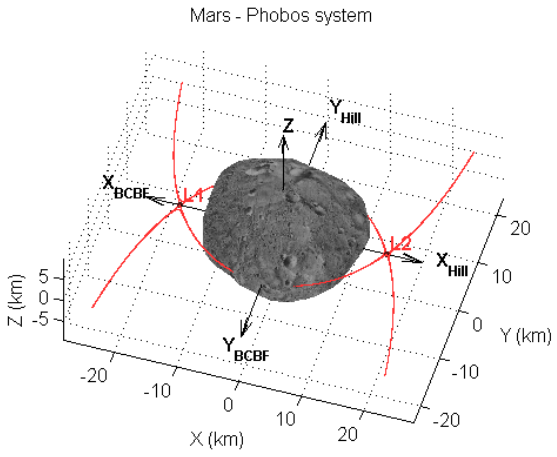

(n,m)	$C_{n,m}$	$S_{n,m}$
(2,0)	-0.04698	0
(2,1)	0.00136	0.00138
(2,2)	0.02276	-0.000202
(3,0)	0.00293	0
(3,1)	-0.00309	0.00181
(3,2)	-0.00847	-0.000655
(3,3)	0.00224	-0.01392
(4,0)	0.00762	0
(4,1)	0.00347	-0.000776
(4,2)	-0.00288	-0.00112
(4,3)	-0.0028	0.00337
(4,4)	-0.0012	-0.000622

Figure 3: Phobos reference frames, CRTBP Lagrangian Points L1, L2 and associated in-plane zero-velocity curves (left), gravity harmonics coefficients [9] (right)

Mars non-spherical gravitational perturbation, and in particular its first zonal coefficient J_2 due to the planet's oblateness, also has a non-negligible contribution, but it remains one order of magnitude below the aforementioned perturbations for the application considered.

The previous figure also illustrates the reference frames used in the study:

- The Hill's frame has its origin at the moon's barycentre and rotates with a fixed attitude with respect to its orbit around Mars: the vertical z-axis is perpendicular to the orbital plane, and the radial x-axis is pointing outwards from the Mars-Phobos barycentre. This is the usual frame considered for the description of the motion in a three-body problem.
- The Body-Centred Body-Fixed frame (BCBF) also has its origin at the moon's barycentre but its attitude is fixed with respect to the body's geometry: the vertical z-axis is aligned along the body's spin axis, and the x-axis is pointing towards the intersection of a body's reference Prime Meridian and the equatorial plane.

As a long-term effect of Mars' gravity gradient (tidal force), Phobos has the interesting property that its revolution around Mars and rotation around its spin axis are synchronous, and almost non-tilted: Phobos is said to be *tidally locked*, like our Moon, always showing the same face to the planet. With this approximation, Hill and BCBF frames z-axes are coincident, while their x-axes differ only by the definition of the Prime Meridian. In particular, Phobos' Prime Meridian is formally identified by the location of the point constantly pointing towards Mars on the body's equator: therefore the two frames differ by a rotation of 180 deg of their x-y plane's axes. In reality, an additional oscillation between a minimum of 0.30 deg and a maximum of 1.90 deg is observed. However the dynamics of this motion, seen from Phobos as a Mars' libration in latitude is much slower (period of 2.26 terrestrial years) than the time-scale of a mission segment around Phobos. [10]

3.2. Dynamics models: Mission Analysis and Guidance (MAG) and Dynamics, Kinematics and Environment (DKE)

The BCBF frame is the most natural coordinate system to be used for a landing problem, and will serve as the reference frame for the expression of the equations of motion, as well as all subsequent trajectory representations in

the next sections. As the main challenge to be addressed in the context of the study is the derivation of robust closed-loop landing strategies in perturbed and poorly known environments, two different models for the descent and landing have been implemented:

- A first model represents the dynamics environment that would be used on the ground for the mission analysis, the definition and design of sets of reference landing trajectories. Assumed to be representative enough of the dynamics in flight, this is also the model to be used by the on-board guidance function. Therefore, this model will be referred to as the *Mission Analysis and Guidance* (MAG) model.

- As the dynamics in orbit will differ from the dynamics predicted on the ground, and in order to be able to assess the robustness of closed-loop landing guidance and control, a second model is needed to simulate the *actual* dynamics experienced by the spacecraft. This model will be referred to as the *Dynamics, Kinematics and Environment* (DKE). This model is a statistical model with some parameters drawn from predefined probability distributions: each DKE simulation is therefore a single realisation of the statistical model. It also includes second order perturbations such as Mars' J_2 and Mars' libration apparent motion from Phobos's BCBF frame.

Based on the previous description of the various contributors to the orbital dynamics in the vicinity of Phobos, the table 2 summarises the assumptions considered for each of these models.

The equations of motion are fairly complex to account for all the effects described above, and further detail is provided in [10]. However, they can be written in a compact and generic state-space form, with the state vector $\underline{X}$ (BCBF position and velocity), vector field f (MAG or DKE), command matrix B and propulsive acceleration $\underline{U}$, as:

$$\dot{\underline{X}} = f(\underline{X}, t) + B \cdot \underline{U} \tag{3}$$

	Dynamics model	
Contributors	MAG	DKE
Mars gravity model	Keplerian (Spherical potential)	Kepler + J_2 (GHs = first zonal coefficient)
BCBF wrt Hill	Fixed and non-tilted (equatorial)	Librating
Phobos gravity model	Full GHs ($m = 4, n = 4$) Deterministic	Full GHs ($m = 4, n = 4$) Probabilistic
Probabilistic parameters	None	GHs coefficients $C_{n,m}$ and $S_{n,m}$ $\mathcal{N}(\mu_{\text{MAG}}, \sigma = 100\%\|\mu_{\text{MAG}}\|)$

Table 2: Differences in assumptions for the MAG and DKE dynamics models

Due to Phobos' orbit ellipticity, the system is non autonomous and it must be augmented with an equation for Phobos true anomaly ν on its orbit around Mars. This standalone equation can be written as follows, e being Phobos' orbit eccentricity and n its mean motion:

$$\dot{\nu} = n\frac{(1 + e\cos(\nu))^2}{(1 - e^2)^{3/2}} \tag{4}$$

3.3. Initial guess for landing trajectories using Libration Point Orbits and invariant manifolds

As described in the previous paragraph, it is impossible to design an orbit around Phobos that is not strongly perturbed by the gravity of Mars. Therefore, instead of using distant Quasi-Satellite Orbits (QSOs) for the selection of the landing site, followed by a sequence of costly forced manoeuvres for the descent and landing, the solution investigated in this study consists in using Libration Point Orbits (LPOs) as natural close observation platforms, and their invariant manifolds, initiated by a small magnitude ΔV on the LPO, as an *initial guess* for a landing trajectory. In order to simulate such trajectories, the first step is to derive the conditions for suitable LPOs. The derivation of Periodic Orbits [11, 12] (POs) and Quasi-Periodic Orbits [13, 14] (QPOs) in the CRTBP has

been studied extensively in the past. The figure 4 below illustrates families of Lyapunov planar, vertical and Halo periodic orbits around the L1 and L2 Lagrangian Points of the Mars-Phobos system. However, such orbits are unstable and, as the dynamics is strongly perturbed, trying to remain on an LPO computed in the CRTBP would come at a significant station-keeping cost. The procedure used [8] is to *identify* LPOs in the Mars-Phobos-spacecraft CRTBP and then numerically continue a parameter that incrementally increases the effect of perturbations: the gravity harmonics and then the eccentricity. Eventually, families of POs, Quasi-Halo and Lissajous QPOs are derived in the full MAG nonlinear dynamical system. The invariant manifolds associated with all these orbits are then computed and those intersecting with Phobos are selected, as illustrated by the figure 4 below.

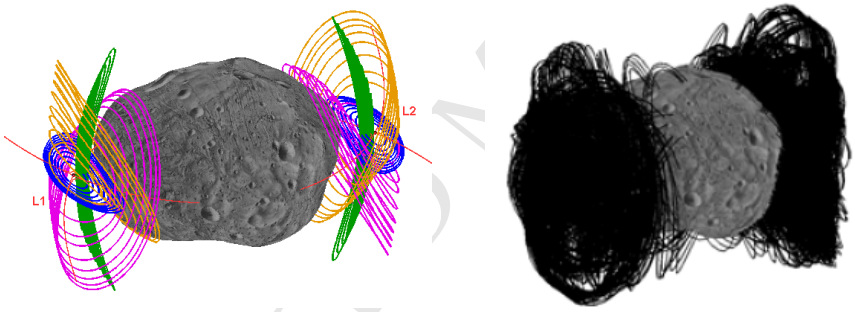

Figure 4: Families of L1 and L2 POs (left), and LPO manifolds interesecting Phobos (right)

The procedure used to derive the invariant manifolds associated with a Periodic Orbit of a nonlinear dynamical system consists in propagating numerically the State Transition Matrix together with the equations of motion. The *monodromy matrix* is then obtained by evaluating this matrix after a full period. The analysis of the eigenspace of the monodromy matrix provides the initial conditions to reach the unstable manifolds associated with the orbit, in practice by applying a very small ΔV in a direction derived from the eigenvectors. For further details on the implementation of this technique to the derivation of trajectories in proximity of Phobos, the reader is referred to [10].

If the landing site is not imposed, several trajectories are generally suitable

candidates, and can be filtered according to an additional criterion. On the example considered, for each reachable landing site, the manifold with the highest incidence at touch-down (the most vertical) is selected. Finally the landing site is chosen as the one with the lowest touch-down velocity.

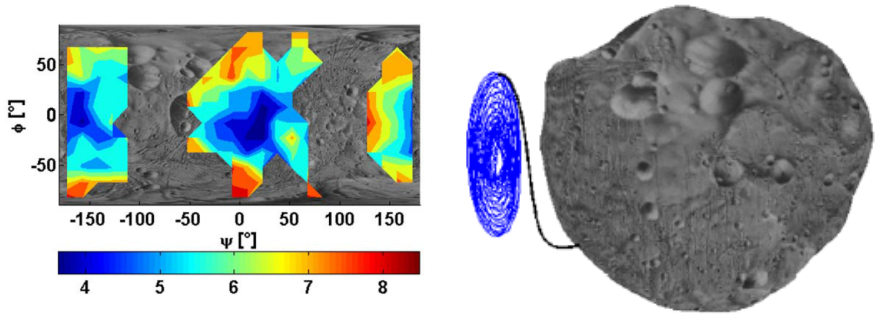

Figure 5: Touch-down velocity map (left) and selected manifold (right)

3.4. Soft landing manifold trajectory optimisation

As the previously described ballistic manifold trajectory does not achieve a soft landing (zero velocity at touch-down), the next step consists in implementing thrust to command the spacecraft to the landing site, described by the position vector $\underline{r}_f$, with no final velocity, i.e. $\underline{v}_f = 0$.[6] The Open-Loop Guidance (OLG) profile is searched as a fixed order polynomial expression between a start time t_b and and a final time $t_f > t_b$, with time normalised by Phobos orbital period T.

$$\underline{U}(t > t_b) = \sum_{k=0}^{n} \underline{U}_k \left(\frac{t - t_b}{T} \right)^k \tag{5}$$

Such a fixed structure parametrisation of the OLG profile will lead to a suboptimal solution, but it has two important advantages: first, it is easy to

[6] In the context of this work, no final free fall requirement has been considered for the derivation of the Open-Loop Guidance and subsequent closed-loop tests. This is without loss of generality as it would only modify the numerical values for the target position $\underline{r}_f$ and velocity $\underline{v}_f$, the free fall problem being addressed separately.

implement in an on-board software, and besides it allows using parametric Non-linear Programming (NLP) algorithms with a reduced set of parameters, for a faster optimisation process. An interior-point method [15] has been used to solve the optimisation problem, with a convergence in the order of a few seconds. The optimisation parameters are the polynomial coefficients of the propulsive acceleration, as well as the burn start (t_b) and end (t_f) dates. The objective is to minimise the propulsive ΔV, while keeping an admissible level of error on the final state, enforced as constraints on the final position and velocity errors, with tolerance derived from the landing accuracy requirements. Conservative assumptions of $\Delta r_{tol} = 10$ m and $\Delta v_{tol} = 10$ cm/s have been considered. The formulation of the optimisation problem can be summarised as follows:

$$\begin{aligned} &\min_{t_b, t_f, \{\underline{U}_k\}_{k\in[\![0,n]\!]}} J(t_b, t_f, \{\underline{U}_k\}_{k\in[\![0,n]\!]}) = \int_{t_0}^{t_f} \|\underline{U}(t)\| dt \\ &\text{Landing accuracy constraints: } \begin{cases} \|\underline{r}(t_f) - \underline{r}_f\| < \Delta r_{tol} \\ \|\underline{v}(t_f) - \underline{v}_f\| < \Delta v_{tol} \end{cases} \end{aligned} \tag{6}$$

Figure 6 illustrates the solution trajectory reached, using the ballistic manifold described in the previous section as the initial guess ($\underline{U}_k = 0$, $t_b = 0$, t_f = impact time of the ballistic manifold). Arrows represent the direction and relative magnitude of the optimal OLG propulsive acceleration: the thrusters are activated as soon as the spacecraft leaves the Libration Point Orbit ($t_b = 0$).

Figure 7 shows the velocity profile, driven to 0 at the final time, compared to the initial guess ballistic trajectory, and the optimised command profile. The optimised open-loop soft landing has a duration of less than 2 hours and requires a propulsive ΔV of about 7 m/s.

Local optima were reached by the optimiser with different values of $t_b > 0$, when initialised with initial guesses far from t_0. However, as a general rule, and despite the fact that the thrust duration is less, the required propulsive acceleration is significantly increased, and its time integral, which corresponds to the propulsive ΔV, is increased as well.

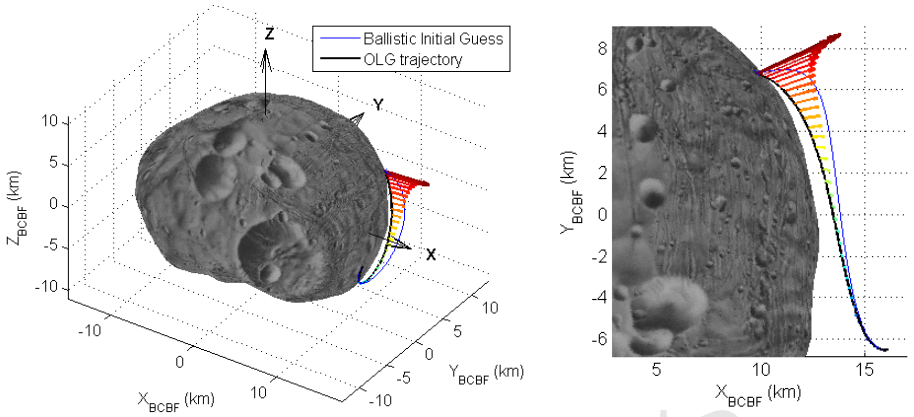

Figure 6: Manifold landing trajectory: the black line represents the trajectory and the coloured arrows the optimised propulsive acceleration profile.

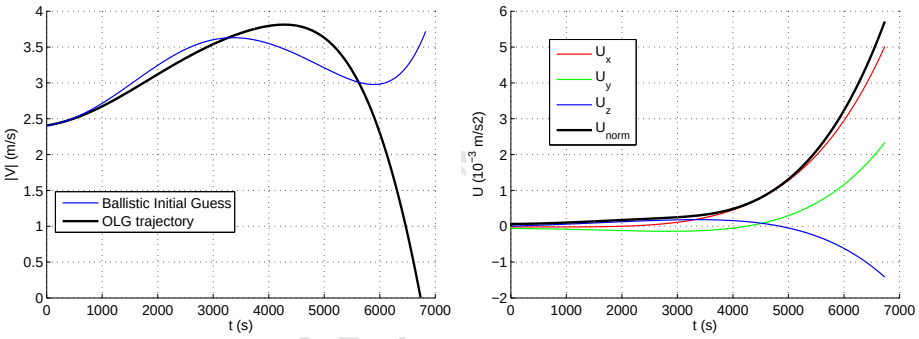

Figure 7: Optimised OLG manifold landing velocity (left) and command (right) profiles

3.5. Forced translation descent trajectory optimisation

In order to compare the manifold-based landing to a more classical approach, a second open-loop reference trajectory is computed as a forced translation from a hovering Station-Keeping (SK) point 10 km above the surface towards the same landing site, along the local normal to the surface.

This case is easier since a parametric analytical expression of the reference *kinematics* can be given so as to meet the soft landing requirement. The trajectory to follow is a straight line from the initial hovering position to the targeted landing site. However, the velocity profile to be followed by the spacecraft along this straight line can be optimised. Starting with a velocity equal to 0, and aim-

ing for a zero velocity at the final time, a simple admissible solution is given by a trapezoidal profile: ramping up between t_0 and Δt_1 until the spacecraft reaches the maximum descent velocity v_d, then ramping down between $t_f - \Delta t_2$ and t_f to reach $v_f = 0$. This velocity profile can be described by only four parameters $(\Delta t_1,\ \Delta t_2,\ v_d,\ t_f)$ that fully define the descent kinematics: by integration of this continuous piecewise function, one can derive the analytical expression of the position vector, with initial, final and continuity constraints used to derive the integration constants. Table 3 below summarises these expressions.

Time	Position	Velocity	Acceleration
$[t_0, \Delta t_1]$	$\underline{r}(t) = \underline{r}_0 + \frac{\underline{v}_d t^2}{2\Delta t_1}$	$\underline{v}(t) = \frac{\underline{v}_d t}{\Delta t_1}$	$\underline{a}(t) = \frac{\underline{v}_d}{\Delta t_1}$
$[\Delta t_1, t_f - \Delta t_2]$	$\underline{r}(t) = \underline{r}_0 + \underline{v}_d \left(t - \frac{\Delta t_1}{2} \right)$	$\underline{v}(t) = \underline{v}_d$	$\underline{a}(t) = 0$
$[t_f - \Delta t_2, t_f]$	$\underline{r}(t) = \underline{r}_f - \frac{\underline{v}_d (t_f - t)^2}{2\Delta t_2}$	$\underline{v}(t) = \frac{\underline{v}_d (t_f - t)}{\Delta t_2}$	$\underline{a}(t) = -\frac{\underline{v}_d}{\Delta t_2}$

Table 3: Kinematics equations for the forced translation

An additional constraint is imposed by the continuity of the position of the spacecraft at $t = t_f - \Delta t_2$, reducing the number of free parameters down to three. This constraint is expressed as:

$$\underline{v}_d = \frac{\underline{r}_f - \underline{r}_0}{t_f - \left(\frac{\Delta t_1 + \Delta t_2}{2} \right)} \tag{7}$$

The propulsive acceleration required is obtained as the difference between the total acceleration and the apparent gravitational acceleration given by the MAG vector field velocity components:

$$\underline{U}(t) = \underline{a}(t) - f_v(\underline{X}, t) \tag{8}$$

This time the soft landing requirement is ensured by design, and the ΔV minimisation problem to solve can be written again as a parametric minimisation problem, with a single inequality:

$$\min_{\Delta t_1, \Delta t_2, t_f \geq \Delta t_1 + \Delta t_2} J(\Delta t_1, \Delta t_2, t_f) = \int_{t_0}^{t_f} \|\underline{U}(t)\| dt \tag{9}$$

Figure 8 illustrates the solution trajectory, the arrows representing the direction and relative magnitude of the optimal OLG propulsive acceleration.

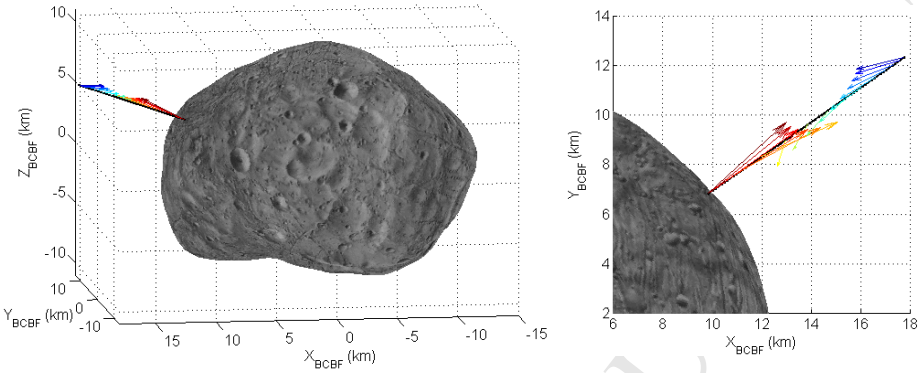

Figure 8: Forced translation landing: the black line represents the trajectory and the coloured arrows the optimised propulsive acceleration profile.

The illustrated forced translation landing has a duration of less than 1 hour and requires a propulsive ΔV of about 16.5 m/s, which is significantly higher than the previous manifold-based trajectory. In addition, the hovering station-keeping point needs to be maintained prior to landing, at an average[7] cost of about 50 m/s per Phobos orbital period or 6.9 m/s per hour.

Figure 9 shows again the velocity profile, and the optimised command profile. The reached solution is such that the trapezoidal velocity profile degenerates into a triangular profile with $\Delta t_1 + \Delta t_2 = t_f$ (active inequality constraint), as shown by the left figure.

4. Closed-Loop Guidance implementation

In the previous section, open-loop command profiles (referred to as Open-Loop Guidance OLG) have been optimised and simulated in the dynamics environment described by the MAG model. As expected, when injected in an

[7] The instantaneous SK cost depends on Phobos true anomaly, and the spacecraft's altitude, latitude and longitude.

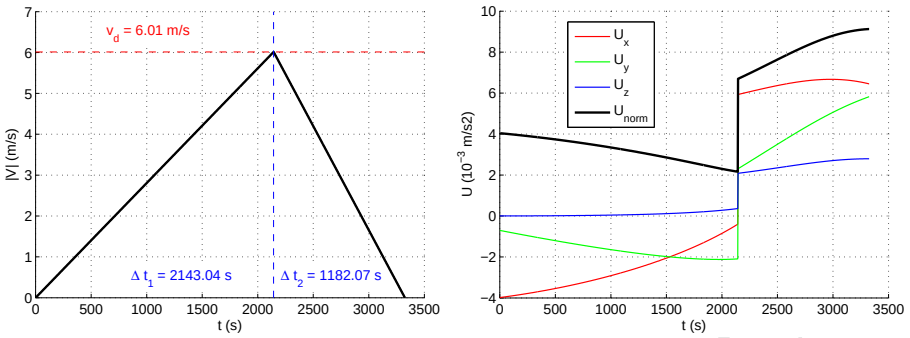

Figure 9: Forced translation landing velocity (left) and command (right): the optimisation leads to a triangular velocity profile without any coast arc.

instance of the DKE model to simulate the *actual* dynamics experienced by the spacecraft, the OLG command profile generally steers the spacecraft on a trajectory that rapidly diverges from the nominal trajectory. Figure 10 illustrates the observed behaviour when simulating the manifold-based OLG in a Monte-Carlo campaign of 200 DKE runs: as summarised in table 2, the Gravity Harmonics of Phobos are drawn from a Gaussian distribution with mean values identical as those of the MAG model (see figure 3), and standard deviations equal to the absolute value of the corresponding coefficients. As evidenced by the left figure, some trajectories will actually crash on Phobos and some others will never reach its surface (single DKE realisation example on the right, with OLG command profile), demonstrating the importance of the considered perturbations on the dynamics, and calling for the implementation of robust closed-loop guidance strategies.

4.1. Guidance problem

The role of the *guidance* function is to compute, from the estimation of the current state of the spacecraft, the command and associated trajectory to follow so as to meet the mission's objectives, while respecting a given set of constraints and generally optimising a performance index. This function can be implemented either on the ground or directly in the on-board software, with a variety of possible intermediate architectures and subsequent impacts on the

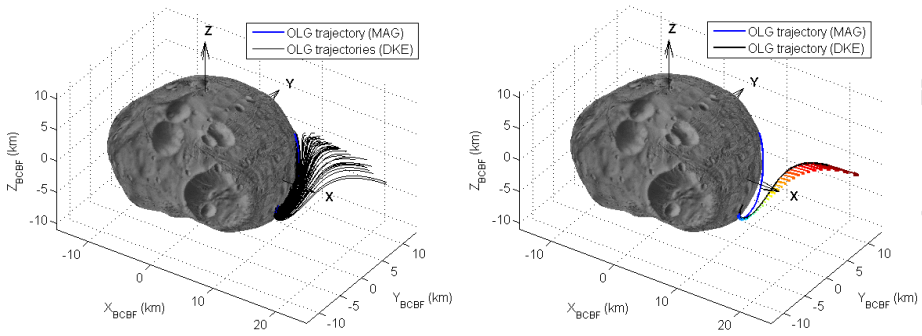

Figure 10: DKE simulations: the left figure shows the possible trajectories for various instances of the DKE (Monte-Carlo), the right figure illustrates the example of one that escapes Phobos when using the manifold landing trajectory OLG command profile (coloured arrows, derived using the MAG model) in one realisation of the DKE.

overall concept of operations. In the context of the present study, the objective is to maximise the autonomy of the spacecraft for the descent and landing phase: given the possibly long communication delays[8] as compared to the landing phase duration, the spacecraft should be able to complete its mission autonomously as soon as the descent is initiated.

Ideally, the guidance optimisation problem solved in real-time should be the same optimisation problem as the one considered for the mission analysis on the ground before the mission for the derivation of reference trajectories, only replacing the initial state by the actual (estimated) state at the current guidance step. Such an approach, sometimes called *fully explicit* Closed-Loop Guidance (CLG), is illustrated by the block-diagram 11 below: in this case the pre-computed OLG profile is not used, or only to initialise the optimisation process. At the extreme opposite, a *fully implicit* strategy would use directly the OLG with no feedback of the estimated state to recalculate the command, which has been demonstrated to be inapplicable for our problem.

[8]Depending on the orbital configuration of the planets, round-trip communication times between the Earth and Mars can take from under 10 minutes up to more than 40 minutes.

[9]The control allocation and navigation functions are not described in this paper, as they

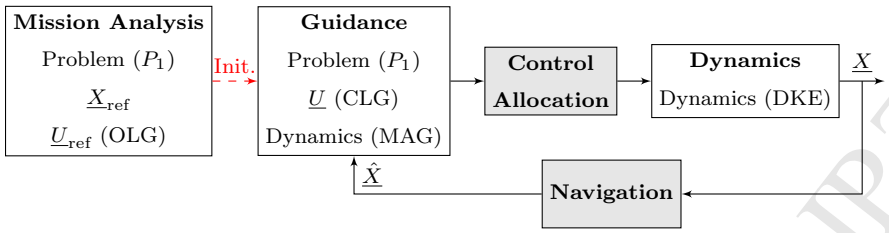

Figure 11: Fully explicit Closed-Loop Guidance (CLG) architecture[9]

In most cases however, the resolution of the full optimisation problem is not compatible with the on-board computational resources and/or time constraints, so that the guidance optimisation problem must be simplified. This simplification can arise from the description of the dynamics, the expression of the constraints, or even the selection of the performance index.

A typical example for a space trajectory guidance strategy is to use a quadratic performance index, instead of a more natural cost functional that would be associated with the propellant consumption. Let us consider two optimisation problems (P_1) and (P_2), characterised by distinct cost functionals $J_{\mathcal{L}_1}$ and $J_{\mathcal{L}_2}$, defined respectively as the $\mathcal{L}_1$ and $\mathcal{L}_2$ norms of the control:

$$J_{\mathcal{L}_1}(\underline{U}) = \int_{t_0}^{t_f} \|\underline{U}(t)\| dt \quad ; \quad J_{\mathcal{L}_2}(\underline{U}) = \int_{t_0}^{t_f} \|\underline{U}\|^2(t) dt \tag{10}$$

The appendix provides a simple example of a dynamical system for which both problems can be solved analytically, minimising respectively $J_{\mathcal{L}_1}$ and $J_{\mathcal{L}_2}$, and illustrating some characteristic differences between the two corresponding types of solutions. For a realistic space trajectory optimisation problem, there is no such analytical solution, however in general:

- From a mission perspective, $\mathcal{L}_1$ is a more appropriate definition of the actuation cost: it is directly associated with the propulsive ΔV, and therefore the propellant consumption. Such problems are generally challenging

are very system-dependent: respectively on the propulsion system and thruster configuration, and the sensor suite and estimation algorithms, which are not the object of the study.

to solve, characterised by non-smooth solutions[10], requiring iterative and highly computationally demanding methods. Reference OLG in the previous sections have been derived using $\mathcal{L}_1$ cost functionals.

- Conversely, quadratic ($\mathcal{L}_2$) optimisation problems are generally easier to solve numerically (smooth solutions) and in case the dynamics is simple, analytical solutions may even be found.

As a consequence, quadratic ($\mathcal{L}_2$) optimisation problems are generally well adapted for on-board closed-loop guidance schemes, while minimum propellant consumption $\mathcal{L}_1$ optimisation problems are considered for the derivation of initial reference trajectories, part of the Mission Analysis commanding profile derivation calculated on the ground. However, as illustrated by the simple example in the appendix, penalties are expected to be incurred from the resolution by the guidance function of a distinct (easier) optimisation problem.

4.2. Guidance survey for autonomous planetary landing

Closed-loop guidance for autonomous landing has been the focus of several studies in the past twenty years. Most state-of-practice techniques provide simple analytical command laws, derived by considering highly simplified exogenous conditions, such as constant or time-explicit gravitational acceleration. Moreover, optimality is not always sought or achieved with respect to a quadratic performance index and no path constraint. Some of these guidance schemes are reported in the table 4 and further described in [16].

- The first, known as Proportional Navigation Guidance (PNG), inspired by the missile interception problem, aims at driving the Line-Of-Sight (LOS) rate to zero by applying an acceleration perpendicularly to the LOS direction $\underline{\Lambda}$ and proportional to the closing velocity V_c. The coefficient k is a tunable parameter known as the effective navigation ratio [17].

[10]The fact that the solutions are singular does not mean that they are not achievable: saturated *bang-bang* like optimal control solutions may actually be more representative of the physical operating of a spacecraft propulsion system.

Proportional Navigation Guidance (PNG)	$\underline{U} = kV_c\underline{\dot{\Lambda}}$
Augmented PNG (APNG)	$\underline{U} = kV_c\underline{\dot{\Lambda}} - \frac{k}{2}\underline{g}_{\perp}$
Biased PNG (BPNG)	$\underline{U} = 4V_c\underline{\dot{\Lambda}} - \underline{g} + \frac{2V_c}{t_{\mathrm{go}}}(\underline{\Lambda} - \underline{\Lambda}_f)$
Free Terminal Velocity (FTVG)	$\underline{U} = \frac{3}{t_{\mathrm{go}}^2}(\underline{r}_f - \underline{r}) - \frac{3}{t_{\mathrm{go}}}\underline{v} - \frac{3}{2}\underline{g}$
Constrained Terminal Velocity (CTVG)	$\underline{U} = \frac{6}{t_{\mathrm{go}}^2}(\underline{r}_f - \underline{r}) - \frac{4}{t_{\mathrm{go}}}\underline{v} - \underline{g} - \frac{2}{t_{\mathrm{go}}}\underline{v}_f$
FTVG ZEM-ZEV formulation	$\underline{U} = \frac{3}{t_{\mathrm{go}}^2}\underline{ZEM}$
CTVG ZEM-ZEV formulation	$\underline{U} = \frac{6}{t_{\mathrm{go}}^2}\underline{ZEM} - \frac{2}{t_{\mathrm{go}}}\underline{ZEV}$

Table 4: Classical and optimal autonomous guidance schemes analytical expressions

- The Augmented PNG (APNG) variant accounts for the contribution of a constant gravity field, and the Biased PNG (BPNG) constrains the terminal LOS to $\underline{\Lambda}_f$ [18]. The latter involves the *time-to-go* $t_{\mathrm{go}} = t_f - t$, defined as the remaining duration until the end of the manoeuvre.

- Free (FTVG) and Constrained (CTVG) Terminal Velocity Guidance are solutions of a quadratic optimal control problem, with no path constraint, assuming a constant gravity field $\underline{g}$ [19, 20, 21]. These can be equivalently formulated in terms of *Zero Effort Miss* (ZEM) and *Zero Effort Velocity* (ZEV), respectively defined as the final errors in position and velocity if no command was to be applied after the current date:

$$\underline{ZEM}(t) = \underline{r}_f - \underline{r}(t_f)|_{\underline{U}(\tau\in[t,t_f])=\underline{0}} \quad ; \quad \underline{ZEV}(t) = \underline{v}_f - \underline{v}(t_f)|_{\underline{U}(\tau\in[t,t_f])=\underline{0}} \tag{11}$$

4.3. Guidance implementation and preliminary results

Among the above guidance schemes, the Constrained Terminal Velocity Guidance (CTVG) is the most appropriate as it results from an optimal control problem formulation with a fixed final *full* state, including the velocity. Its direct implementation in the closed-loop model including the *DKE* dynamics can be performed by taking at each guidance step t: the apparent gravitational acceleration given by the *MAG* vector field velocity components at the estimated current state $\underline{g} = f_v(\underline{\hat{X}}, t)$, and the remaining time until the end of the *reference* open-loop trajectory as the time-to-go. Considering perfect navigation

and actuation as well as a time-continuous closed-loop guidance correction for a preliminary assessment, the trajectory meets the landing requirements, reaching the target at zero velocity with a good accuracy. However, the results exhibit some significant limitations associated with this direct implementation:

- The impossibility to include some path constraints on the trajectory implies that it is not possible to prevent trajectories that would theoretically reach the desired final state with intermediate positions passing below the surface of Phobos, actually leading to a crash.
- As anticipated in the previous paragraph, the ΔV required to follow the trajectory is significantly increased as compared to the OLG reference.[11]

Figure 12 illustrates such an example, starting from the initial conditions of the manifold-based trajectory, but following a very different path and crashing into Phobos. The ΔV is 15.4 m/s, which is more than twice the OLG ΔV.

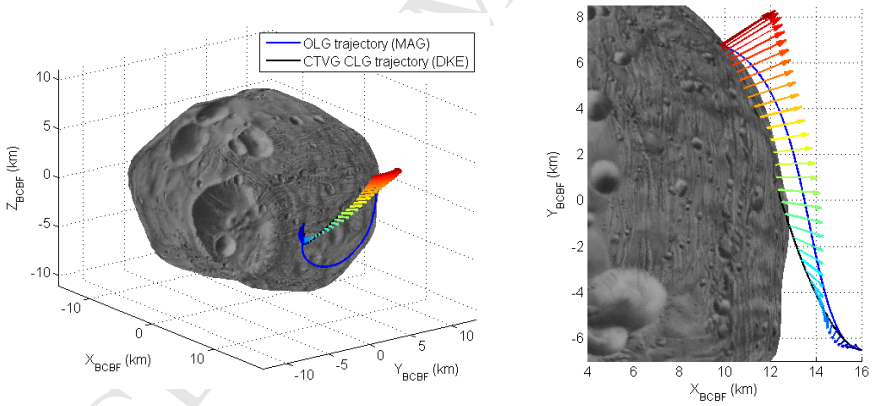

Figure 12: Crashing trajectory DKE simulation: the direct implementation of the CTVG law does not consider any path constraint, such as maintaining a positive altitude.

Both limitations can be addressed by an adaptation of the guidance strategy,

[11] In the CTVG formulation, the final time t_f is fixed, so that a one-dimensional optimisation (line search) of this parameter could be performed as part of the guidance update. However this would lead to consider again an iterative algorithm that was avoided by using an analytical solution of a pre-solved problem.

illustrated by the figure 13. Instead of targeting at each *guidance step* the *final* reference date and state (landing site with zero-velocity), the time-to-go, or *guidance horizon* (between the current date and the target date), can be reduced to target an intermediary state interpolated on the reference trajectory.

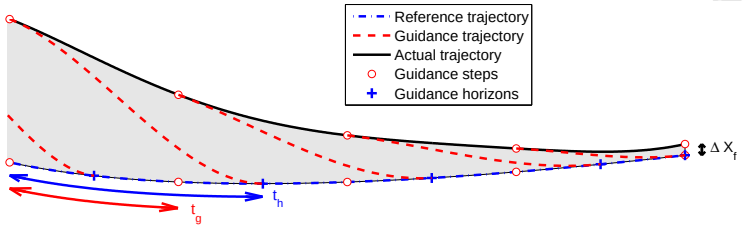

Figure 13: Waypoint based CTVG schematic principle: the targets are intermediary points on the reference trajectory.

A parametric analysis of this strategy has been performed for a range of *guidance steps* t_g and *guidance horizons* $t_h \geq t_g$, still assuming perfect navigation and actuation to focus on the guidance. The CTVG trajectory illustrated earlier then becomes a special case of this generalised *waypoint based* CTVG algorithm, with a guidance horizon equal to the full time-to-go until landing and a continuous guidance correction of the trajectory. The accuracy can be measured by the 2-norm of a vector defined by the (normalised) error on the position and velocity at the nominal final time t_f.[12]

$$J(\Delta r_f, \Delta v_f) = \left\| \left(\frac{\Delta r_f}{\Delta r_{\text{tol}}}, \frac{\Delta v_f}{\Delta v_{\text{tol}}} \right) \right\|_2 = \sqrt{\left(\frac{\Delta r_f}{\Delta r_{\text{tol}}} \right)^2 + \left(\frac{\Delta v_f}{\Delta v_{\text{tol}}} \right)^2} \tag{12}$$

A few points on the (t_g, t_h) domain have been selected for further analysis, to derive some statistics (mean value and standard deviation) for the the propulsive ΔV and final accuracy, drawn from a Monte-Carlo analysis on the DKE model

[12] While the state errors at time t_f and the derived J performance index do indeed measure the *guidance* performance as a deviation from the nominal target in state and time, it is not necessarily representative of actual trajectories, as some will have crashed before t_f, and some others may very well reach the surface of Phobos at a later date.

realisations, and reported in the tables 5. The normalising values of $\Delta r_{\text{tol}} = 10$ m and $\Delta v_{\text{tol}} = 10$ cm/s have been used.

$\mu[\Delta V]$ (m/s)		t_g (s)				$\sigma[\Delta V]$ (m/s)		t_g (s)			
		10	100	200	400			10	100	200	400
t_h (s)	1000	7.34	7.36	7.36	7.66	t_h (s)	1000	0.96	0.96	0.95	1.10
	2000	8.07	8.16	8.23	8.39		2000	1.05	1.08	1.12	1.08
	3000	9.91	10.1	10.3	10.9		3000	1.13	1.17	1.23	1.27

$\mu[J]$ (-)		t_g (s)				$\sigma[J]$ (-)		t_g (s)			
		10	100	200	400			10	100	200	400
t_h (s)	1000	0.17	0.55	0.68	4.71	t_h (s)	1000	0.09	0.26	0.57	2.04
	2000	0.15	0.52	0.51	4.63		2000	0.09	0.39	0.41	2.81
	3000	0.13	0.45	0.53	5.55		3000	0.09	0.32	0.39	3.71

Table 5: Parametric analysis of the waypoint based CTVG: performance (ΔV) and accuracy (position and velocity) statistics are derived from a DKE Monte-Carlo campaign for various values of the guidance frequency and time horizon.

As could be expected, the results show that the guidance performance is increased for a higher correction frequency (small t_g), which in practice will be limited by the on-board computational time and the delays involved in the overall closed-loop. Regarding the guidance horizon, shorter times for $t_h > t_g$ are better for the ΔV, almost asymptotically reaching the reference OLG ΔV, with a lesser impact on the final accuracy, up to a certain limit when the closed-loop becomes unstable and the trajectories diverge from the reference.

5. Conclusion

This paper presented the work conducted by Airbus Defence and Space and the University of Bristol on strategies for autonomous landing on small bodies, with a focus on the mission analysis, reference trajectory optimisation, and preliminary closed-loop guidance assessment. The reformulation of the guidance problem as a tracking-like problem opens the door for a range of control theory applications. By implementing an inner control loop of a linearised model of the dynamics in the vicinity of the reference trajectory, as shown schematically

by the block-diagram on figure 14, several techniques for the synthesis, tuning and analysis from modern robust control theory [22, 23, 24] become applicable, and their application to landing on Phobos have been described in a dedicated paper [16].

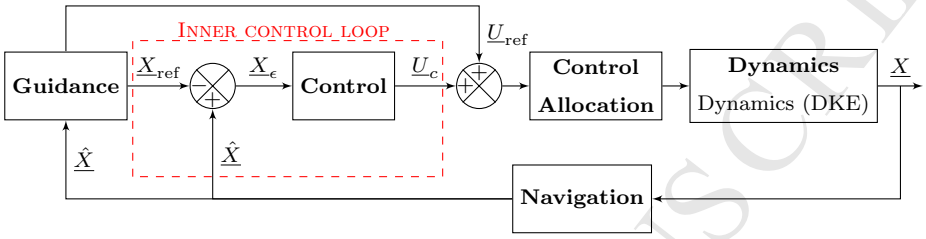

Figure 14: Architecture with control inner loop: the reformulation of the guidance problem as a tracking-like problem opens the door for a wide range of linear control theory applications.

Further selection among of the various architectures and options demonstrated to perform properly for an actual Phobos Sample Return mission will be subject to a more detailed set of requirements for the Guidance, Navigation and Control subsystem as the project hopefully progresses to an implementation phase. In particular, the detailed modelling and performance of the navigation, control allocation and thruster modulation functions as well as other system-level constraints could narrow down the range of possible techniques.

In the challenging framework of a landing on Phobos, Libration Point Orbits have been computed and proposed to be used as natural observation platforms, while their associated manifolds serve as initial guess for optimising a controlled landing trajectory towards a selected landing site. Owing to limited on-board resources, the guidance function considers a simpler optimisation problem, at the expense of an increased propellant consumption. This can however be mitigated by making the most of the reference trajectory in a waypoint based adaptation of a quadratic optimal guidance scheme. Overall, the strategy proved to be compliant with the surface access requirements, and to cope with highly complex and uncertain dynamics environments, achieving a significant reduction of the propellant consumption when compared to more classical approaches.

6. Acknowledgement

This work has been funded by the UK Space Agency, under the National Space Technology Programme. The authors are thankful to Mick Johnson and Christopher Brownsword, respectively Director and Technical Director of the Centre for Earth Observation and Instrumentation (CEOI), for their support and collaboration in the first months of the project, as well as Barbara Richardson, NSTP Programme Manager and coordinating the project for the UKSA.

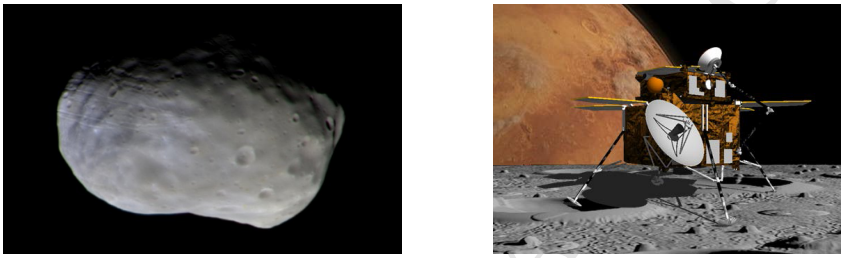

Figure 15: Colour composite of Phobos taken by ExoMars TGO in November 2016 (left) [Credits: ESA/Roscosmos/CaSSIS] and artist's view of a Phobos Lander (right)

Appendix A. Notation

μ_g	Gravity constant = GM
U_g	Gravity field scalar potential
r	Orbital radius (wrt Phobos)
θ	Co-latitude
ϕ	Longitude
$C_{n,m}$, $S_{n,m}$	Cosinus and Sinus Gravity Harmonics coefficients
$\mu[A]$	Mean value (of a random variable A)
$\sigma[A]$	Standard deviation (of a random variable A)
$\mathcal{N}(\mu, \sigma)$	Gaussian distribution with mean μ and standard deviation σ
$\underline{X}$	State vector: position and velocity relative to Phobos BCBF
$f(\underline{X}, t)$	Dynamics vector field (MAG or DKE)
e	Phobos orbit eccentricity
n	Phobos orbit mean motion
T	Phobos orbital period
ν	Phobos true anomaly
$\underline{r}$	Spacecraft position (Phobos BCBF)
$\underline{v}$	Spacecraft velocity (Phobos BCBF)
$\underline{a}$	Spacecraft acceleration (Phobos BCBF)
$\underline{U}$	Command vector: propulsive acceleration
k	Effective navigation ratio (PNG guidance algorithm)
$\underline{\Lambda}$	Line-Of-Sight (LOS) vector
V_c	Closing velocity (relative to the target)
t_{go}	Time-to-go
$\underline{ZEM}$	Zero-Effort-Miss
$\underline{ZEV}$	Zero-Effort-Velocity

Appendix B. $\mathcal{L}_1$ and $\mathcal{L}_2$ optimal control double integrator example

In this appendix, the difference between *propellant* optimal ($\mathcal{L}_1$) and *energy* optimal ($\mathcal{L}_2$) control problems is illustrated on the double integrator archetypal example of a normalised mechanical system, with bounded control:

$$\dot{\underline{X}} = f(\underline{X}, \underline{U}) \text{ , with } \begin{cases} \underline{X} &= [x_1, x_2]^T \\ \underline{U} &= u \in [-u_{max}, +u_{max}] \\ f(\underline{X}, \underline{U}) &= [x_2, u]^T \end{cases} \tag{B.1}$$

In this example, x_1 is the scalar position of the system, $x_2 = \dot{x_1}$ is the velocity, and the acceleration $\ddot{x_1}$ is directly equal to the input command u that drives the system. For a standard *rendezvous* problem with zero initial (and final) velocity with fixed terminal time t_f, we must have in addition:

$$\underline{X}(t_0) = [a, 0]^T \quad ; \quad \underline{X}(t_f) = [b, 0]^T \tag{B.2}$$

We consider two unconstrained optimisation problems (P_1) and (P_2), characterised by distinct cost functionals $J_{\mathcal{L}_1}$ and $J_{\mathcal{L}_2}$, defined respectively as the $\mathcal{L}_1$ and $\mathcal{L}_2$ norms of the control function:

$$(P_1) \ : \ J_{\mathcal{L}_1}(u) = \int_{t_0}^{t_f} |u(t)| dt \quad ; \quad (P_2) \ : \ J_{\mathcal{L}_2}(u) = \int_{t_0}^{t_f} u^2(t) dt \tag{B.3}$$

The advantage of the simple dynamical system considered is that analytical solutions can be derived for both optimal control problems, illustrated on the figure B.16 for $u_{max} = 1$, $t_f = 10$, $a = 0$, $b = 10$. As evidenced by the table B.6, controls ${u^*}_{\mathcal{L}_1}$ and ${u^*}_{\mathcal{L}_2}$ are only optimal for their respective problems, the solution of (P_1) (resp. (P_2)) minimising the cost functional $J_{\mathcal{L}_1}$ (resp. $J_{\mathcal{L}_2}$).

Problem	Optimal control	Functional $J_{\mathcal{L}_1}$	Functional $J_{\mathcal{L}_2}$
(P_1)	${u^*}_{\mathcal{L}_1}$	**2.25**	2.25
(P_2)	${u^*}_{\mathcal{L}_2}$	3.00	**1.20**

Table B.6: $\mathcal{L}_1$ and $\mathcal{L}_2$ costs of (P_1) and (P_2) solutions

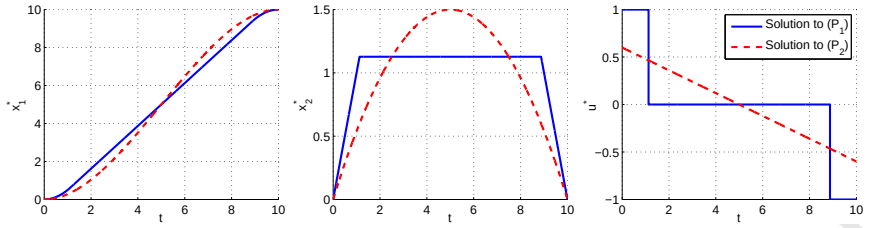

Figure B.16: Optimal position $x_1{}^*$, velocity $x_2{}^*$ and command u^* profiles for problems (P_1) and (P_2)

This example illustrates some fundamental differences between $L1$ and $L2$ categories of optimal control problems, with a smooth solution for the quadratic problem, and a discontinuous *bang-bang* solution for the $L1$ problem: to the limit where $u_{max} \to \infty$ (unbounded control), L1 optimal control would tend to a couple of symmetric Dirac distributions at t_0 and t_f, corresponding to the model of impulsive (instantaneous) velocity increments, and asymptotic cost $J_{\mathcal{L}_1} = 2(b-a)/t_f = 2.00$.

References

[1] Z. Junjun, N. Dauphas, A. Davis, I. Leya, A. Fedkin, The proto-earth as a significant source of lunar material., Nature Geoscience 5 (4) (2012) 251 – 255.

[2] L. Peacocke, M. C. Perkinson, J. Reed, M. Wolf, T. Lutz, C. Balemboy, Terminal descent and landing architectures for a mars precision lander, in: 8th International Planetary Probe Workshop, 2011.

[3] L. Peacocke, S. Kemble, M. Chapuy, H. Scheer, MarcoPolo-R: Mission and Spacecraft Design, European Planetary Science Congress 2013 8 (2013) EPSC2013–116.

[4] S. Barraclough, A. Ratcliffe, R. Buchwald, H. Scheer, M. Chapuy, M. Garland, D. Rebuffat, Phootprint: A european phobos sample return mission,

in: 11th International Planetary Probe Workshop, Vol. 1795 of LPI Contributions, 2014, p. 8030.

[5] T. Duxbury, J. Callahan, Pole and prime meridian expressions for phobos and deimos., Astronomical Journal 86 (11) (1981) 1722 – 1727.

[6] V. Szebehely, Theory of orbit : The restricted problem of three Bodies., Academic Press, 2012.

[7] M. Zamaro, J. D. Biggs, Identification of new orbits to enable future mission opportunities for the human exploration of the martian moon phobos., Acta Astronautica 119 (2016) 160 – 182.

[8] M. Zamaro, J. D. Biggs, Dynamical systems techniques for designing libration point orbits in proximity of highly-inhomogeneous planetary satellites: Application to the mars-phobos elliptic three-body problem with additional gravity harmonics., AIP Conference Proceedings 1637 (1) (2014) 1228 – 1240.

[9] B. F. Chao, D. P. Rubincam, The gravitational field of phobos, Geophysical Research Letters 16 (8) (1989) 859–862. doi:10.1029/GL016i008p00859.

[10] M. Zamaro, Natural and artificial orbits around the martian moon phobos, Ph.D. thesis, University of Strathclyde (10 2015).

[11] R. Farquhar, The control and use of libration-point satellites. (1968) 214.

[12] K. Howell, Three-dimensional, periodic, 'halo' orbits., Celestial Mechanics 32 (1) (1984) 53 – 71.

[13] J. M. Mondelo González, G. Gómez, The dynamics around the collinear equilibrium points of the rtbp.

[14] E. Kolemen, N. Kasdin, P. Gurfil, Multiple poincare sections method for finding the quasiperiodic orbits of the restricted three body problem., Celestial Mechanics and Dynamical Astronomy 112 (1) (2012) 47 – 74.

[15] R. H. Byrd, M. E. Hribar, J. Nocedal, An interior point algorithm for large-scale nonlinear programming, SIAM Journal on Optimization 9 (4) (1999) 877900. doi:10.1137/s1052623497325107.

[16] P. Simplicio, A. Marcos, E. Joffre, M. Zamaro, N. Silva, Synthesis and analysis of robust control compensators for space descent and landing, International Journal of Robust and Nonlinear Control (May 2018). doi:10.1002/rnc.4109.

[17] P. Zarchan, Tactical and Strategic Missile Guidance Sixth Edition., American Institute of Aeronautics & Astronautics, 2012.

[18] K. Byung Soo, L. Jang Gyu, H. Hyung Seok, Biased png law for impact with angular constraint., IEEE Transactions on Aerospace and Electronic Systems 34 (1) (1998) 277 – 288.

[19] M. Hawkins, Y. Guo, B. Wie, Zem/zev feedback guidance application to fuel-efficient orbital maneuvers around an irregular-shaped asteroid., in: Papers - American Institute of Aeronautics and Astronautics, 7th Edition, Vol. 7 of AIAA guidance, navigation, and control conference, 2012, pp. 5745 – 5768.

[20] G. Yanning, M. Hawkins, W. Bong, Applications of generalized zero-effort-miss/zero-effort-velocity feedback guidance algorithm., Journal of Guidance, Control, and Dynamics 36 (3) (2013) 810 – 820.

[21] M. Hawkins, Y. Guo, B. Wie, Guidance algorithms for asteroid intercept missions with precision targeting requirements (aas 11-531)., Advances in the Astronautical Sciences 142 (2012) 1951 – 1970.

[22] A. Falcoz, C. Pittet, S. Bennani, A. Guignard, C. Bayart, B. Frapard, Systematic design methods of robust and structured controllers for satellites., CEAS Space Journal 7 (3) (2015) 319 – 334.

[23] J. Doyle, A. Packard, K. Zhou, Review of lfts, lmis, and mu., Dept. of Electr. Eng., Caltech, Pasadena, CA, USA, 1991.

[24] A. Marcos, S. Bennani, Lpv modeling, analysis and design in space systems: Rationale, objectives and limitations., in: Papers - American Institute of Aeronautics and Astronautics, 1st Edition, Vol. 1 of Guidance, navigation and control, 2009, pp. 286 – 308.

- Description of the dynamics environment in the vicinity of the Martian Moon Phobos
- Derivation of orbits and their manifolds as ballistic initial guesses for landing
- Optimisation of powered landing open-loop reference trajectories
- Survey and implementation of closed-loop guidance strategies
- Monte-Carlo campaign for performance assessment in perturbed environment